



2D Benzodithiophene based conjugated polymer/g-C₃N₄ heterostructures with enhanced photocatalytic activity: Synergistic effect of antibacterial carbazole side chain and main chain copolymerization

Xiaojie Liu^a, Yahui Du^a, Yong Zhao^a, Xin Song^a, Xin Jing^a, Liangmin Yu^{b,d}, Mingliang Sun^{a,b,c,*}

^a School of Materials Science and Engineering, Ocean University of China, Qingdao 266100, China

^b Open Studio for Marine Corrosion and Protection, Pilot National Laboratory for Marine Science and Technology (Qingdao), Qingdao 266100, China

^c Institute of Polymer Optoelectronic Materials and Devices, State Key Laboratory of Luminescent Materials and Devices, South China University of Technology, Guangzhou 510640, China

^d Key Laboratory of Marine Chemistry Theory and Technology, Ministry of Education, Ocean University of China, Qingdao 266100, China

ARTICLE INFO

Keywords:

Donor–acceptor conjugated polymer
Benzodithiophene
Carbazole side chain
Photocatalytic antibacterial
Photocatalytic degradation

ABSTRACT

Constructing polymer heterojunction (PHJ) has emerged as an alternative to pursue excellent photocatalytic sterilization and contaminant degradation performance. Herein, the antibacterial carbazole unit is employed as the side chain of benzodithiophene. Besides, the main chain copolymerization strategy is adopted to tune the light absorption and exciton dissociation of these 2D donor–acceptor (D–A) conjugated polymer/g-C₃N₄ PHJ by introducing different A units. Specifically, copolymerizing diketopyrrolopyrrole into P4 drastically bathochromic-shifts the light absorption of the PHJ. By contrast, introducing fluorinated benzotriazole into P9 contributes to achieve the most efficient charge separation. Surprisingly, the P7/g-C₃N₄ with benzodithiophene-4,8-dione as the A unit reaches the balance between light absorption, charge separation efficiency, and water wettability. Consequently, the P7/g-C₃N₄ shows the highest photocatalytic activity with over 99.7% antibacterial rates for *E. coli* and *S. aureus* and 97.6% degradation rate for Rhodamine B under irradiation for 45 and 90 min, respectively.

1. Introduction

Photocatalysis has drawn more attention in combating with the pathogenic microorganisms and degrading contaminant for tackling the global water pollution issues [1–4]. Heretofore, remarkable efforts have been made on the development of efficient photocatalysts to accelerate the photocatalytic reaction driven by the solar light. For a long time, the inorganic semiconductors as key photocatalysts have occupied the predominant position among the intensively investigated systems, which mainly include metal-oxides [5,6], metal-sulfides [7,8], and metal-nitrides [9,10] etc. Nevertheless, the toxicity of metals associated with inorganic photocatalysts is still an obstacle that hinders their further large-scale applications. Thus, metal-free photocatalysts have drawn great attention in recent years because of their attractive environmental benignity and satisfactory earth-abundance. Graphitic carbon nitride (g-C₃N₄), a state-of-the-art representative of metal-free

photocatalysts, has been extensively studied in the field of photocatalysis owing to excellent chemical and thermal stability and facile manufacturing process [11–14]. However, the relatively large band gap (E_g) of g-C₃N₄ (about 2.7 eV) limits its light absorption and the high exciton binding energy of the photo-generated Frenkel excitons leads to low dissociation probabilities and rapid recombination of charges [15–17]. To address these shortcomings and optimize the photo-electrochemical properties of g-C₃N₄, strenuous efforts have been made. In various strategies, constructing heterostructures has been regarded as one of the most effective methods, which could not only broaden light absorption but also facilitate charge separation and migration [18–20].

π -conjugated polymers with versatile physicochemical properties have appeared as another potential candidates for photocatalysis [21, 22]. The rational molecular design could endow the conjugated polymers with specific chemical functions, leading to a wider range of photocatalytic applications. To match well with the solar photon flux

* Corresponding author at: School of Materials Science and Engineering, Ocean University of China, Qingdao 266100, China.

E-mail address: milsun@ouc.edu.cn (M. Sun).

<https://doi.org/10.1016/j.apcatb.2022.121401>

Received 10 February 2022; Received in revised form 27 March 2022; Accepted 8 April 2022

Available online 12 April 2022

0926-3373/© 2022 Elsevier B.V. All rights reserved.

spectrum, extensive studies have been conducted on the synthesis of narrow E_g organic semiconductors in recent years. Utilizing D (electron-donating unit)–A (electron-accepting unit) copolymerization in the main chain engineering has been reported as the most efficient strategy to adjust the E_g and absorption spectra of the polymers to make better use of sunlight with long wavelength [23–25]. The virtues of D–A conjugated polymers and g-C₃N₄ have inspired the researchers to fabricate D–A polymers/g-C₃N₄ polymer heterostructures. Among them, the poly-fluorene family polymers (PFs)/g-C₃N₄ PHJs have been widely developed [26–28]. However, the photocatalytic activities, especially the apparent quantum yield values of PFs/g-C₃N₄ were not ideal because of the poor visible light response and unsatisfactory electron hole separation efficiency. Consequently, it is significant to further broaden the light absorption and promote the carrier separation efficiency of conjugated polymers/g-C₃N₄.

Over the past decade, the conjugated polymers with benzodithiophene (BDT) as the D unit have been witnessed great success in designing highly efficient photovoltaic materials [29,30]. The large planar conjugated structure, easily formed π - π stacking, and small steric hindrance of the BDT units are beneficial to the charge transfer in the BDT polymers: fullerene or nonfullerene heterojunctions leading to high power conversion efficiencies [29,31]. In the side chain engineering, the conjugated side chains are always employed to optimize the structure of BDT to synthesize 2D-BDT polymers and obtain better photoelectrochemical properties. Carbazole is a traditional electron-donating unit with wide E_g and the introduction of carbazole side chain could broaden the absorption of polymers in the visible and ultraviolet region. This strategy combining with the D–A copolymerization in the main chain engineering is favorable for realizing the absorption of the whole solar spectrum. In our previous work, we have synthesized the 2D carbazole side-chained BDT-based conjugated polymers P5 and P7 with the 4,7-di(4-(2-ethylhexyl)–2-thienyl)–5,6-difluoro-2,1,3-benzothiadiazole (DTffBT) and benzodithiophene-4,8-dione (BDD) as A units, respectively [32]. Encouragingly, these two polymers showed excellent photoelectric conversion performance in applications for organic solar cells. Moreover, it has been reported that the carbazole and its derivatives possess antibacterial activities [33,34]. Therefore, it is reasonable to expect the high performance of the carbazole side-chained BDT-based conjugated polymers in the photocatalytic sterilization and degradation.

Herein, four 2D conjugated polymers (P4, P5, P7, and P9) utilizing carbazole side-chained BDT as the D unit and diketopyrrolopyrrole (DPP), DTffBT, BDD, and fluorinated benzotriazole (FBTA) with diminishing electron-accepting ability as A units were synthesized. Further, the P4/g-C₃N₄, P5/g-C₃N₄, P7/g-C₃N₄, and P9/g-C₃N₄ PHJs were successfully constructed for photocatalytic sterilization and degradation for the first time. Undoubtedly, the relatively strong electron-withdrawing ability of DPP promoted the intramolecular charge transfer of P4, bathochromic-shifting the absorption edges of P4/g-C₃N₄ to 860 nm, while the P9/g-C₃N₄ realized the most efficient charge separation. Nevertheless, the P7/g-C₃N₄ achieved the balance of light absorption, charge separation efficiency, and water wettability, resulting in the best photocatalytic performance for sterilization and degrading contaminant. In addition, the active species trapping experiment, electron spin resonance (ESR) test, and density functional theory (DFT) calculations have been conducted to investigate the photocatalytic mechanism of Px/g-C₃N₄ PHJs (x = 4, 5, 7, and 9).

2. Experimental

2.1. Materials

The tris(dibenzylideneacetone)dipalladium (Pd₂(dba)₃) and tris(2-methylphenyl) phosphine(P(o-tol)₃) were purchased from Shanghai Darui Chemicals Co., Ltd. DPP, DTffBT, BDD, and FBTA were obtained from Derthon Optoelectronics Materials Science Technology Co., Ltd.

Urea, *p*-hydroxyphenylacetic acid (POHPAA), horseradish peroxidase, potassium hydrogen phthalate, isopropanol (IPA), sodium oxalate, 4-hydroxy-2,2,6,6-tetramethylpiperidinyloxy (TEMPOL), Rhodamine B (RhB), and other analytical grade chemicals were purchased from Sinopharm Chemical Reagent Co., Ltd., China.

2.2. Synthesis of Px

The polymers P5 and P7 were synthesized according to our previous work [32]. The synthetic methods of P4 and P9 (Scheme 1) are similar to those of P5 and P7. Briefly, the 2,2'-(2,6-bis(trimethylstannyl)benzo[1,2-*b*:4,5-*b'*]dithiophene-4,8-diyl)bis(9-(3-hexyldecyl)–9H-carbazole) (monomer1, 129.5 mg, 0.1 mmol), the monomer DPP (80 mg, 0.1 mmol) or the monomer FBTA (80 mg, 0.1 mmol), Pd₂(dba)₃ (1.8 mg) and P(o-tolyl)₃ (3.6 mg) were added to a 25 mL flask. Then the reaction system was sealed followed by three times of air extraction for the further nitrogen protection. Subsequently, the anhydrous toluene (10 mL) was added into the flask, and the mixture was heated to 110 °C to react for 24 h. After cooling to room temperature, the mixture was dropped into the methanol. Subsequently, the precipitate was further purified by Soxhlet extraction with dichloromethane, chloroform and 1,2-dichlorobenzene. After the rotatory evaporation of the solution, the methanol was used for film-forming. The final target product was then dried in a vacuum at 40 °C.

2.3. Fabrication of Px/g-C₃N₄ PHJ

20 g urea in a crucible was calcined in a muffle furnace with the following process: 450 °C for 1 h and then 550 °C for 3 h with the heating rate of 5 °C/min. After cooling to the room temperature, the crude sample was ground and washed with deionized water three times followed by being dried in a vacuum oven at 70 °C for 12 h, thus obtaining the g-C₃N₄. For the fabrication of Px/g-C₃N₄, 1 mg Px and 200 mg g-C₃N₄ were added into 40 mL dichloromethane, and the mixture was constantly stirred in the dark for 24 h. The target heterostructures Px/g-C₃N₄ were then obtained by rotatory evaporation of the solvent and being dried at 40 °C in a vacuum (Scheme 2).

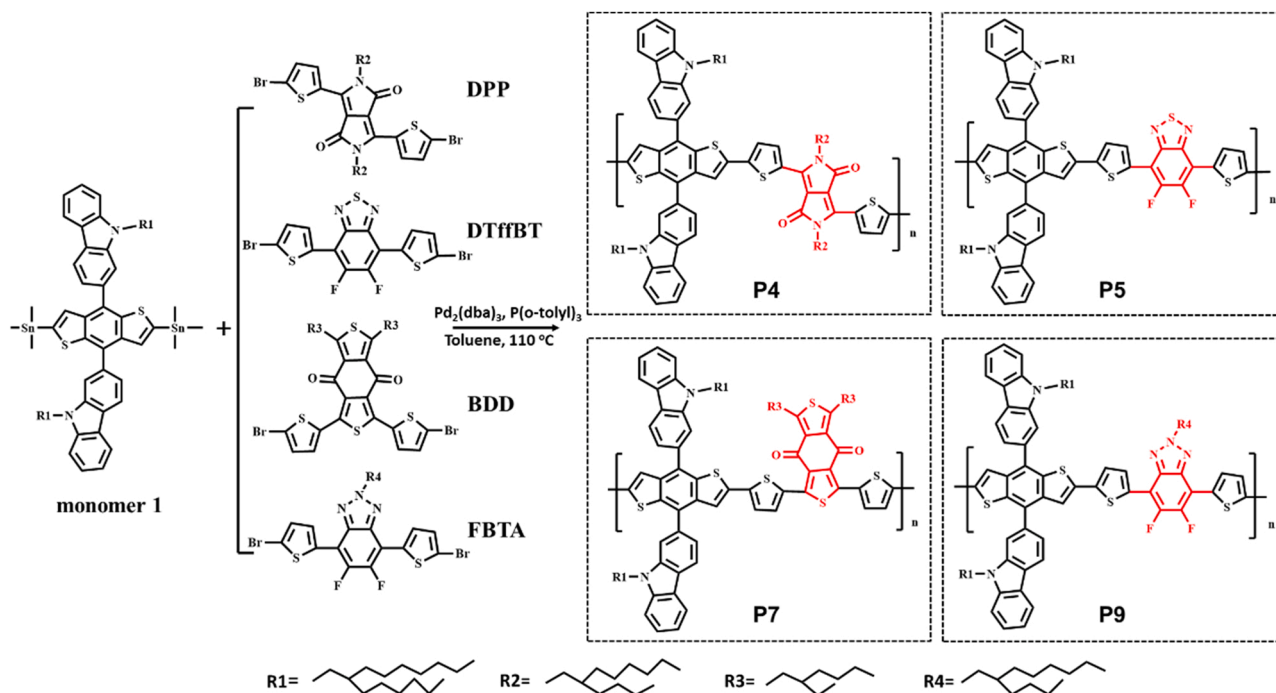
2.4. Photocatalytic performance

The photocatalytic experiments were conducted under an 800 W xenon lamp with 60 mW/cm² light intensity. The wide-type *S. aureus* and *E. coli* were selected as the models to assess the antibacterial effects of the photocatalysts by the plate colony counting method. The survival rate of the bacteria was calculated according to the equation: survival rate (%) = $C_t/C_0 \times 100\%$, where C_0 and C_t represents the number of the bacterial colony at the time of initial and at time *t* under irradiation. In addition, the antibacterial rate was described as: antibacterial rate (%) = 100% - survival rate (%). The details were provided in the Supporting Information.

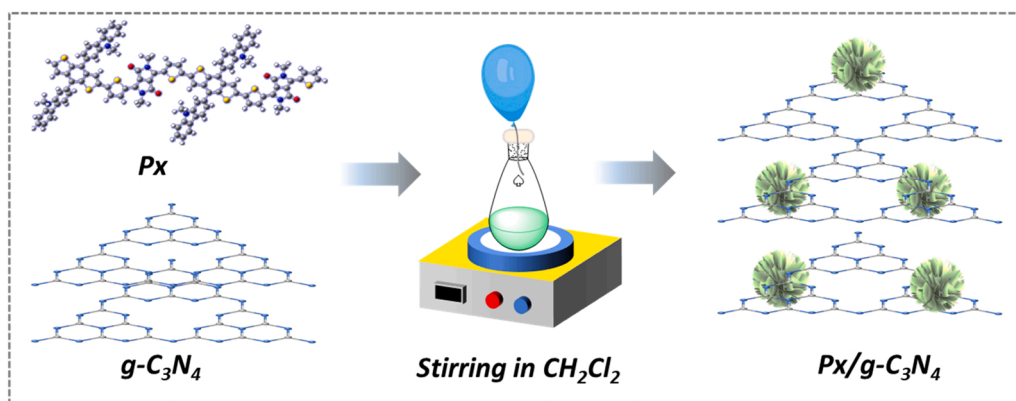
The RhB was selected as the organic contaminant to investigate the photocatalytic activity of the photocatalysts. Typically, 20 mg of the photocatalysts were added into the RhB solution (70 mL, 10 mg/L). Before being irradiated, the suspensions were stirred for 30 min in the dark to achieve the absorption/desorption equilibrium. The concentration of RhB was determined by recording the absorbance of the solution with a spectrophotometer at 554 nm.

2.5. Free radical trapping experiment

To explore the active species that participate in the photocatalytic reactions, the scavengers IPA (10 mM, detecting ·OH), TEMPOL (5 mM, detecting ·O₂), and sodium oxalate (10 mM, detecting of h^+) were added into the reaction systems. The other experimental conditions were the same as those of the photocatalytic sterilization and degradation experiments.



Scheme 1. Synthetic routes of the conjugated polymers P4, P5, P7, and P9.

Scheme 2. Schematic diagram of the fabrication of Px/g-C₃N₄ photocatalysts.

2.6. DFT calculations

The frontier molecular orbitals and intermolecular electrostatic potential (ESP) of the conjugated polymers Px and g-C₃N₄ were calculated using the density functional theory (DFT) method and the corresponding statistics of ESP were collected by Multiwfn [35–38].

3. Results and Discussion

3.1. Characterization

The synthetic routes of Px are shown in Scheme 1. These conjugated polymers were synthesized by Stille polymerization. Four polymers presented good solubility in chloroform and chlorobenzene. The number average molecular weights (*M_n*) of P4, P5, P7, and P9 estimated by the gel permeation chromatography were determined to be 13.8, 50.6, 61.1, and 56.5 kDa, respectively. The scanning electron microscopy (SEM) and transmission electron microscopy (TEM) images (Fig. S1a, b) showed that the g-C₃N₄ possessed a typically fluffy stacking structure with rough edges. In addition, the polymer P4 showed a large sheet

structure with irregular fragments (Fig. S1c) and P5 presented an agglomerate acicular shape (Fig. S1d), while P7 and P9 were characterized with uneven tubular structures (Fig. S1e, f). As indicated from the SEM images (Fig. 1a, d, g, j), the Px/g-C₃N₄ exhibited the similar morphologies to g-C₃N₄ and no specific structure of Px could be observed in the PHJs because of the limited concentration of Px. In the element mapping images (Fig. 1b, e, h, k, and S1g), the distributions of C and N of g-C₃N₄ were in agreement with the SEM image, while the distributions of S, O and F indicated that the Px dispersed uniformly on the surface of g-C₃N₄. In the TEM images, the wide range of brightly colored areas corresponded to g-C₃N₄, while the darker areas belonged to the Px. Compared with the TEM image of g-C₃N₄ in Figure. S1b, the equally distributed dark areas in the TEM images of Px/g-C₃N₄ (Fig. 1c, f, i, l) illustrated the good dispersity of Px. Based on the above characterizations, it could be concluded that the conjugated polymers Px have been successfully anchored on g-C₃N₄ with a uniform dispersion.

The fourier transform infrared spectra (FT-IR) spectra of Px, g-C₃N₄, and the PHJs were analyzed to confirm their molecular structures. As shown in Fig. 2a, all these conjugated polymers showed characteristic peaks at around 1450, 1330, and 3000 cm⁻¹, corresponding to the C=C,

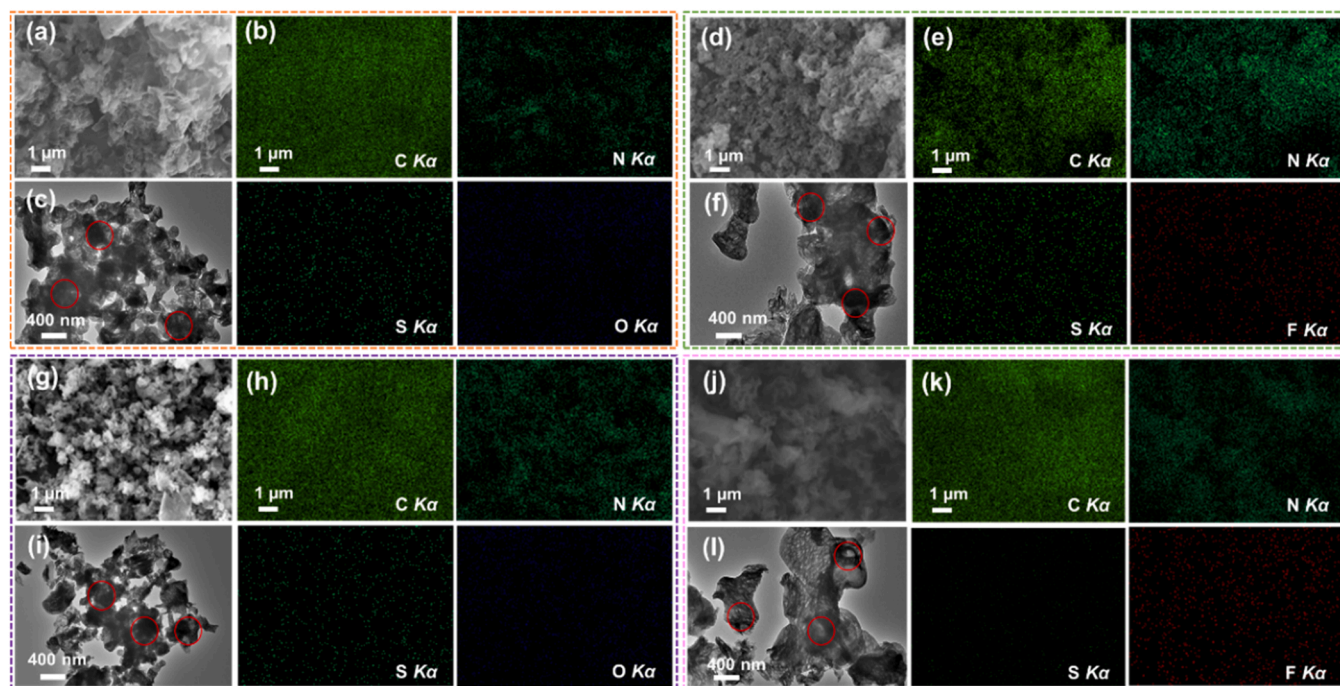


Fig. 1. SEM, EDS elements mapping, and TEM images of P4/g-C₃N₄ (a)–(c); P5/g-C₃N₄ (d)–(f); P7/g-C₃N₄ (g)–(i); P9/g-C₃N₄ (j)–(l).

C—N, and C—H stretching vibrations, respectively [39]. This revealed the existence of the aromatic conjugated D—A skeleton in the polymers. The absorption peaks at around 750–900 and 1000–1250 cm^{−1} belonged to the alkyl C—H rocking mode and bending and twisting, respectively [40], confirming the alkyl chains in the polymers. Further, the stretching vibration signals of C=O at 1665 cm^{−1} could be observed in P4 and P7, while the peaks representing the C—F stretching vibration at 1260 cm^{−1} only existed in P5 and P9, which were in agreement with the chemical structures of target polymers. According to Fig. 2b, the PHJs showed the similar FT-IR spectra to g-C₃N₄, suggesting that the structure of g-C₃N₄ remained integrity. The broad peaks located between 3000 and 3500 cm^{−1} were attributed to the N—H stretching vibrations and O—H vibration originated from the H₂O on the surface of photocatalysts. The characteristic peaks in the range of 1200–1700 cm^{−1} were assigned to the C=N and C—N heterocycles stretching vibrations. Besides, the sharp peak at 808 cm^{−1} was aroused by the bending vibration of the heptazine rings. The crystallinity properties of g-C₃N₄ and Px/g-C₃N₄ were characterized by X-ray diffraction (XRD). As presented in Fig. 2c, the Px/g-C₃N₄ and g-C₃N₄ showed two similar prominent peaks at 13.0° and 27.3°, which were related to the in-plane repeated units and (002) interplanar stacking, respectively [41]. Moreover, there was no special peak of Px in PHJs due to the low loading rates and excellent dispersions of Px. The surface chemical states of the photocatalysts were investigated by X-ray photoelectron spectroscopy (XPS) measurements. Seen from Fig. 2d, the g-C₃N₄ mainly consisted C, N, and a small amount of O element originated from the absorbed H₂O and CO₂, while C, N, O, and S constituted the main elements of Px/g-C₃N₄. Moreover, the F element could only be detected in the P5/g-C₃N₄ and P9/g-C₃N₄, which further demonstrated that the conjugated polymers P5 and P9 coexisted with g-C₃N₄ in PHJs. In the high-resolution spectra of C1s (Fig. 2e), the binding energy of g-C₃N₄ and Px/g-C₃N₄ centered at 284.9 and 288.3 eV corresponded to C=C and C—(N)3, respectively. The N1s spectra were fitted into three peaks at 398.4, 399.1, and 400.4 eV for g-C₃N₄, and 398.7, 399.1, 400.6 eV for Px/g-C₃N₄, which belonged to sp²-hybridized nitrogen C=N—C, N—(C)3, and N—H, respectively (Fig. 2f). Interestingly, compared with the pure g-C₃N₄, the Px/g-C₃N₄ showed a higher binding energy of N1s. It has been reported that the lower binding energy of N1s for the PHJs

indicated the increasing electronic cloud density around the N atoms of g-C₃N₄, which was caused by the intermolecular electron diffusion from the conjugated polymers to the N sites of g-C₃N₄ by the intermolecular π - π interaction [28,40]. Therefore, it was reasonable to attribute the higher shift of the N1s binding energy to the intermolecular electron diffusion from the N sites of g-C₃N₄ to Px. The O1s peaks appeared around 531.8 eV for the g-C₃N₄ due to the adsorbed CO₂, while the peaks at 531.7 and 531.8 eV for PHJs were also caused by the C=O in the polymers (Fig. 2g). The other O1s peaks at 532.9 eV for g-C₃N₄ and around 532.7 eV for the PHJs were related to the hydroxyl group or H₂O. The S2p_{3/2} and S2p_{1/2} peaks of the Px/g-C₃N₄ heterostructures were deconvoluted into 164.0 and 165.3 eV (Fig. 2h). In addition, the observed peaks of 687.4 eV for P5/g-C₃N₄ and P9/g-C₃N₄ were assigned to the introduced F atoms in P5 and P9 (Fig. 2i).

The specific surface areas (SSAs) of the photocatalysts were recorded using the Brunauer–Emmett–Teller (BET) models. Accordingly, the SSAs were determined to be 36.9, 41.1, 43.7, 47.6, and 43.8 m²/g for the g-C₃N₄, P4/g-C₃N₄, P5/g-C₃N₄, P7/g-C₃N₄, and P9/g-C₃N₄, respectively (Fig. 3a). In comparison to the pure g-C₃N₄, the increased SSAs of the PHJs especially that of the P7/g-C₃N₄ contributed to provide more active reaction centers to accelerate the photocatalytic reactions. To investigate the surface wetting properties of the photocatalysts, the contact angles (CAs) with water were measured. As shown in Fig. 3b and S2, the pure g-C₃N₄ exhibited a CA of 38.2°. However, the CAs increased to 67.0°, 46.8°, 54.3°, and 58.8°, respectively, after being coupled P4, P5, P7, and P9 to form the heterostructures because of the hydrophobicity of the conjugated polymers. Significantly, the maximum CA of P4/g-C₃N₄ would reduce the stability of H₂O molecules absorbed on the photocatalysts, resulting in unsatisfactory photocatalytic activity.

3.2. Photoelectrochemical properties

The normalized UV–vis absorption spectra of P4 to P9 are presented in Fig. 3c. The narrower absorption spectra were ascribed to P9 (400–620 nm) and P7 (300–650 nm), while P5 exhibited a strong absorption band from 300 to 750 nm, which covered most of the visible spectrum. Significantly, a strong bathochromic-shift was observed in the absorption spectrum of P4 (500–880 nm). The absorption peaks caused

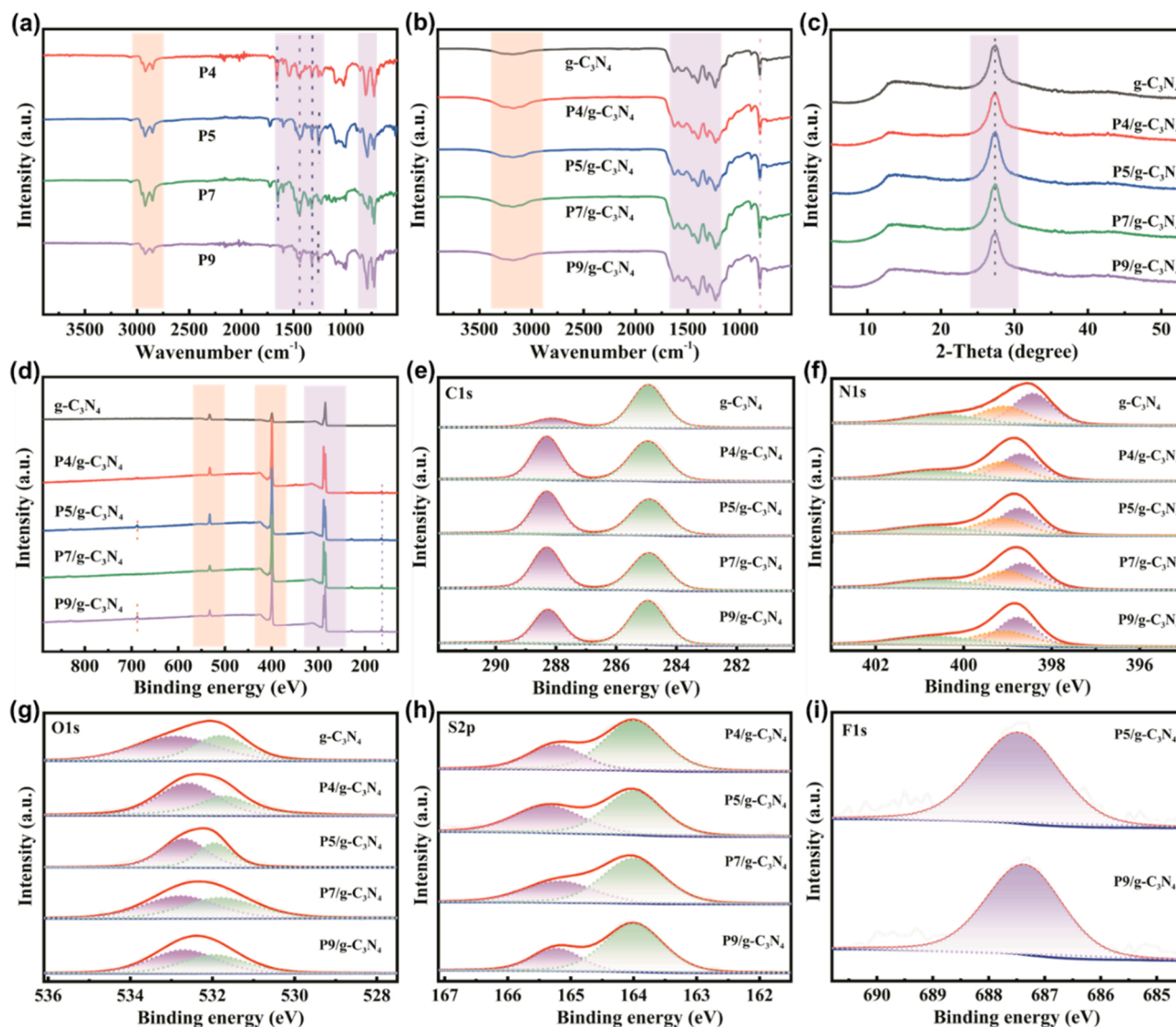


Fig. 2. FT-IR spectra of (a) the conjugated polymers Px and (b) PHJs; (c) XRD patterns of g-C₃N₄ and PHJs; XPS spectra of (d) survey and high-resolution (e) C1s, (f) N1s, (g) O1s, (h) S2p, and (i) F1s spectra for g-C₃N₄ and PHJs.

by the intramolecular charge transfer between the BDT and the A units were around 690, 600, 558, and 530 nm for P4, P5, P7, and P9, respectively, which was in consistent with the electron-withdrawing ability of the A units. In addition, the absorption peaks at about 750, 595, and 575 nm corresponding to P4, P7, and P9 were originated from the inter-chain aggregation absorption. The other minor absorption bands located about 350 nm were assigned to the π - π^* transitions of the conjugated backbones [42]. The UV-vis diffuse reflectance spectra (DRS) test was performed to study the optical properties of the g-C₃N₄ and Px/g-C₃N₄. From Fig. 3d, it could be observed that the conjugated polymers P4 to P9 with high extinction coefficients bathochromic-shifted the absorption edge of the photocatalysts from 450 to 880, 710, 650, and 620 nm, respectively, leading to enhanced light capturing ability. Encouragingly, these Px/g-C₃N₄ are among the most efficient PHJs reported so far in enhancing the light absorption capacity of the g-C₃N₄ with a quite low content of the conjugated polymers (Table S1). Besides, the pictures of the photocatalysts are inserted into Fig. 3d. The optical E_g calculated using Tauc-plots were determined to be 2.87 eV for g-C₃N₄, 1.56 eV for P4, 1.78 eV for P5, 1.98 eV for P7, and 2.06 eV for P9 (Fig. S3), and the corresponding data is summarized in Table 1.

To obtain the oxidation/reduction potentials and estimate the energy

levels of these polymers, the cyclic voltammetry (CV) test was employed. The CV curves and energy level diagram are presented in Figs. 3e and 3f, and the related data are listed in Table 1. The highest occupied molecular orbital (HOMO) levels were calculated by the formula: $HOMO = -e [4.8 + E_{ox,onset}^{sample} - E_{ox,onset}^{Fc/Fc^+}]$ [43]. As shown in Fig. 3e, the onset oxidation potentials $E_{ox,onset}^{sample}$ of the polymers were 1.02 V for P4, 1.12 V for P5, 1.08 V for P7, and 1.01 V for P9, which corresponded to the HOMO energy levels of -5.52, -5.62, -5.58, and -5.51 eV, respectively. Based on the above results, the lowest unoccupied molecular orbital (LUMO) energy levels determined by $LUMO = HOMO + E_g$ were -3.96, -3.84, -3.60, and -3.45 eV, respectively. Moreover, the valence band potential of g-C₃N₄ obtained by the XPS valence band spectrum was determined to be 1.99 V (vs. NHE) that corresponded to the HOMO level of -6.49 eV (vs. vacuum level) (Fig. S4). Based on the CV and XPS measurements, it could be concluded that the Type I band alignments were constructed between g-C₃N₄ and P4 and P5, while the Type II heterostructures were formed between g-C₃N₄ and P7 and P9 (Fig. 3f). To further study the effect of different A units on the molecular energy levels and orbital distributions of the conjugated polymers, theoretical calculations were performed using the DFT method. Here, the long alkyl side chains in the Px were replaced with the methyl groups

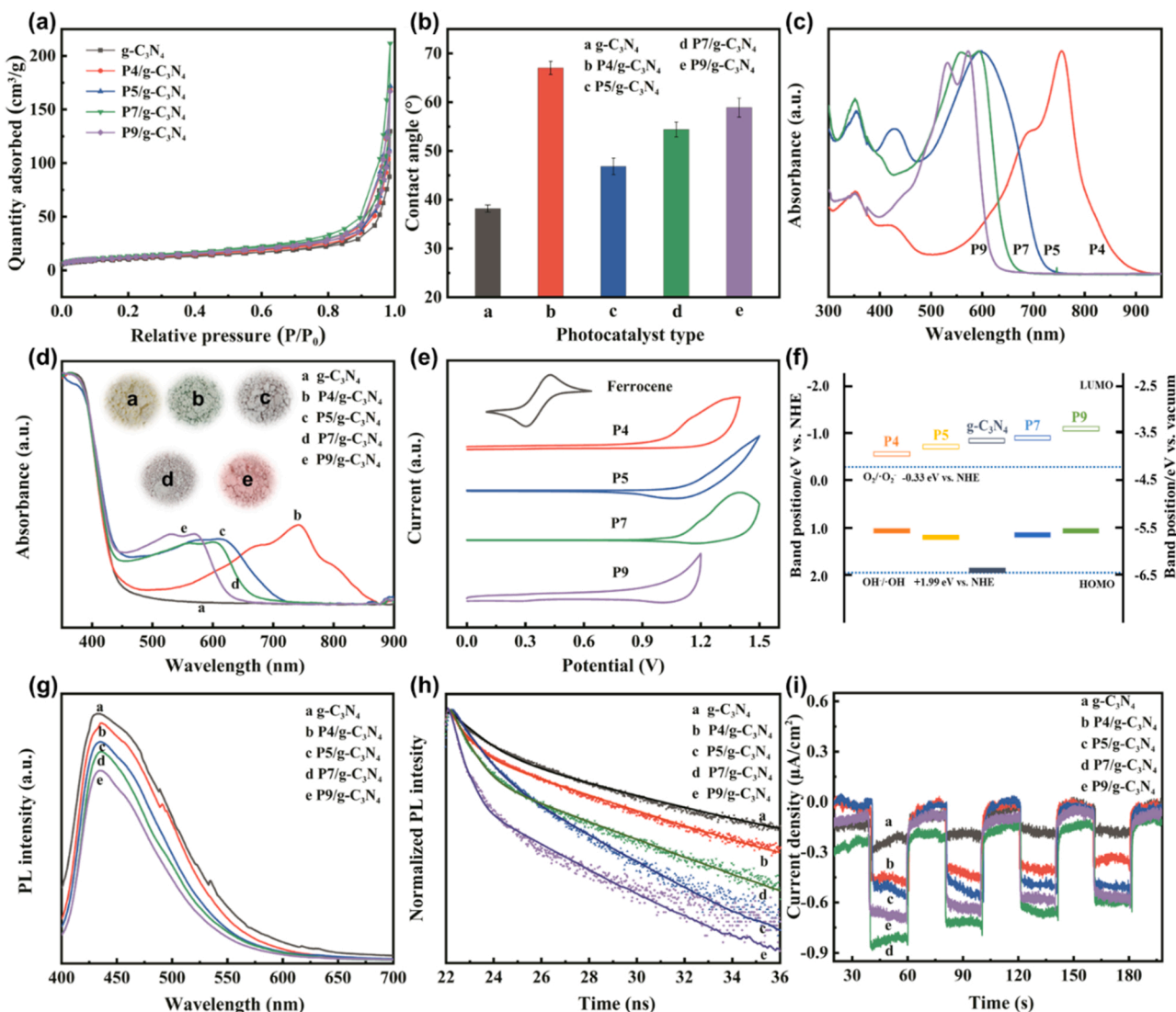


Fig. 3. (a) The nitrogen adsorption–desorption isotherm curves of $g\text{-C}_3\text{N}_4$ and the PHJs; (b) contact angles with water of $g\text{-C}_3\text{N}_4$ and the PHJs; (c) UV–vis absorption spectra of the conjugated polymers Px; (d) UV–vis DRS spectra of $g\text{-C}_3\text{N}_4$ and the PHJs (Inset: the corresponding photographs of the photocatalysts); (e) cyclic voltammetry curves of Px; (f) band alignment of Px and $g\text{-C}_3\text{N}_4$; (g) PL spectra, (h) time-resolved PL decay spectra, and (i) i - t curves of $g\text{-C}_3\text{N}_4$ and the PHJs.

Table 1

Electrochemical properties of the conjugated polymers.

Samples	E_{ox} (vs SHE)(V)	HOMO (eV)	LUMO (eV)	E_g (eV)
P4	1.02	-5.52	-3.96	1.56
P5	1.12	-5.62	-3.84	1.78
P7	1.08	-5.58	-3.60	1.98
P9	1.01	-5.51	-3.45	2.06

to simplify the calculation. Seen from Fig. S5, the HOMO orbitals of the conjugated polymers widely distributed over the D–A main chains, while the LUMO orbitals were mainly localized on the A units. Therefore, in theory the different A units would have greater effects on the LUMO levels of Px. The calculated HOMO levels were -4.76 eV for P4, -4.83 eV for P5, -4.83 eV for P7, and -4.75 eV for P9, and the corresponding LUMO levels were -2.88 , -2.79 , -2.49 , and -2.44 eV, respectively, which were consistent with the trend of CV results.

To investigate the charge mobility of the conjugated polymers, the space charge limited current measurement was conducted. As shown in Fig. S6, the electron and hole mobility were 2.18×10^{-4} and $2.35 \times 10^{-4} \text{ cm}^2 \text{ V}^{-1} \text{ s}^{-1}$ for P4, 4.85×10^{-4} and $1.18 \times 10^{-4} \text{ cm}^2 \text{ V}^{-1}$

s^{-1} for P5, 1.22×10^{-4} and $3.06 \times 10^{-4} \text{ cm}^2 \text{ V}^{-1} \text{ s}^{-1}$ for P7, 2.99×10^{-4} and $2.09 \times 10^{-4} \text{ cm}^2 \text{ V}^{-1} \text{ s}^{-1}$ for P9. The relatively high carrier mobility and balanced ratio of hole/electron mobility of Px contribute to promote the charge transport in Px/ $g\text{-C}_3\text{N}_4$. The photoluminescence (PL) and time-resolved photoluminescence decay (TR-PL) measurements were conducted to investigate the charge separation and transfer behavior of the photocatalysts. As presented in Fig. 3g, a strong PL emission of $g\text{-C}_3\text{N}_4$ at 450 nm could be observed when excited at 385 nm, which represented the distinct recombination of carriers. Nevertheless, this strong PL peak quenched to varying degrees after being constructed heterostructures with the Px, confirming that the carrier recombination was inhibited in the Px/ $g\text{-C}_3\text{N}_4$. Particularly, it needs to be pointed out that the PL intensities of P9/ $g\text{-C}_3\text{N}_4$ and P7/ $g\text{-C}_3\text{N}_4$ were weaker than those of P4/ $g\text{-C}_3\text{N}_4$ and P5/ $g\text{-C}_3\text{N}_4$, indicating that more effective charge transfer occurred in the former, which was favorable for enhancing the photocatalytic performance. As the TR-PL results shown (Fig. 3h), the fluorescence lifetime (τ) of the pure $g\text{-C}_3\text{N}_4$ was 1.74 ns, while the τ of P4/ $g\text{-C}_3\text{N}_4$, P5/ $g\text{-C}_3\text{N}_4$, P7/ $g\text{-C}_3\text{N}_4$, and P9/ $g\text{-C}_3\text{N}_4$ gradually declined to 1.03, 0.84, 0.70, and 0.33 ns, respectively. In general, for the photocatalyst with a single component, a longer τ always represents a more efficient intermolecular charge

separation and transfer, whereas for Px/g-C₃N₄, a shorter τ suggests the formation of the heterostructure and a higher charge extraction from the g-C₃N₄ to Px [43,44]. Therefore, the relative shorter τ of P9/g-C₃N₄ and P7/g-C₃N₄ compared with those of P4/g-C₃N₄ and P5/g-C₃N₄ further demonstrated the faster charge transfer of the former, which was in agreement with the results of PL. The photocurrent densities–time (i–t) curves of g-C₃N₄ and Px/g-C₃N₄ under intermittent light exposure are presented in Fig. 3i. The photocurrent densities of the Px/g-C₃N₄ were all higher than that of g-C₃N₄ because of the enhanced separation and transfer of electron–hole pairs from the g-C₃N₄ to Px. As affected by the light absorption, charge separation and transfer, the photocurrent densities of the photocatalysts were ranked as P7/g-C₃N₄ > P9/g-C₃N₄ > P5/g-C₃N₄ > P4/g-C₃N₄ > g-C₃N₄. The P7/g-C₃N₄ counteracted the

adverse effect of the relatively narrow absorption spectrum and achieved the balance between these two parameters, leading to the highest photocurrent density.

3.3. Photocatalytic performance

3.3.1. Photocatalytic antibacterial performance

The antibacterial performances of g-C₃N₄ and Px/g-C₃N₄ are illustrated in Fig. 4a–d. It could be observed that the antibacterial activities of the blank groups toward *E. coli* and *S. aureus* were negligible in the dark. Nevertheless, a few bacteria were inactivated after being exposed to light, which indicated that the light source may have a slight effect on the survival of bacteria (Figs. 4a and 4c). Additionally, the g-C₃N₄ made

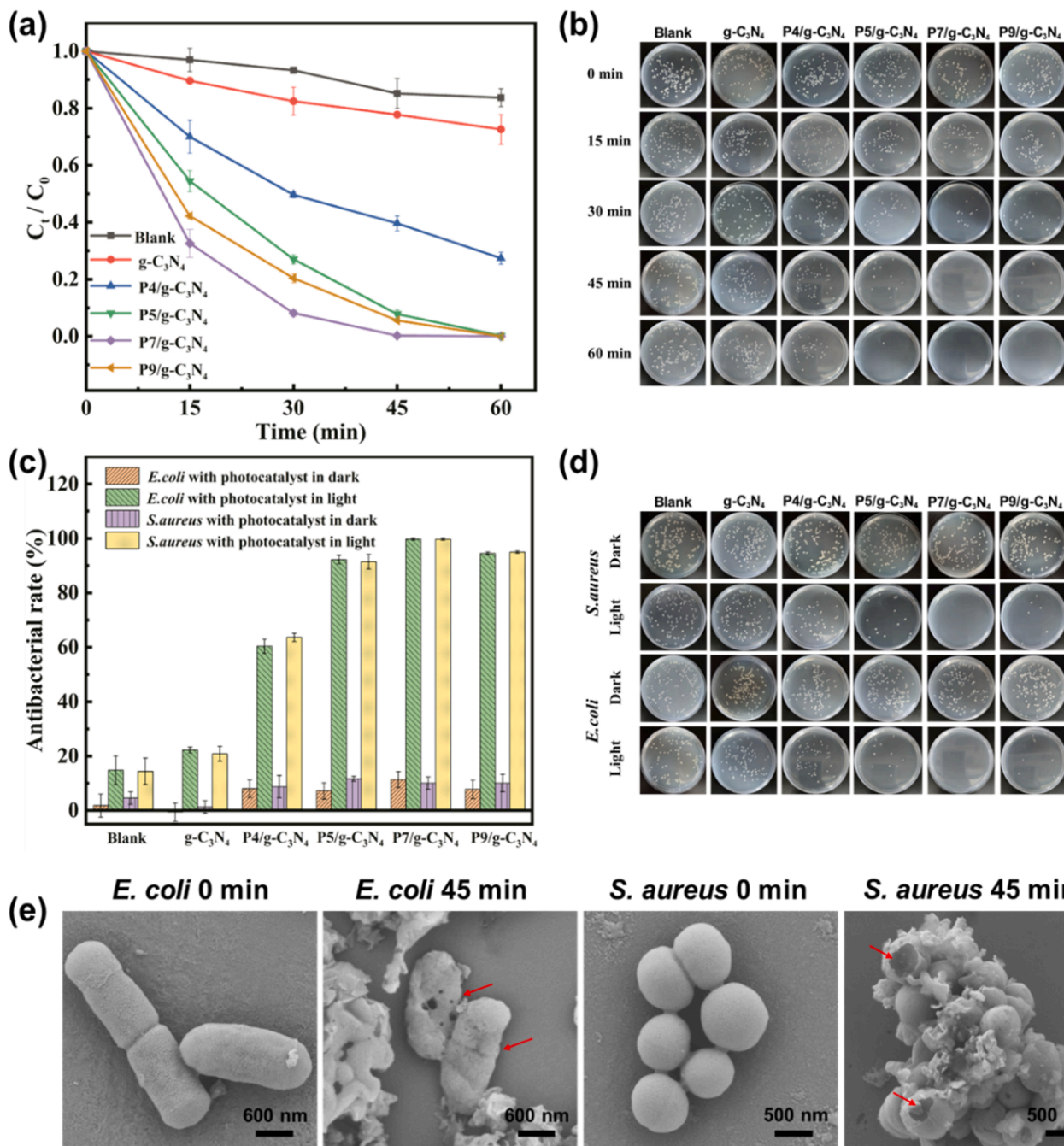


Fig. 4. (a) The temporary survival rate curves and (b) photographs of *E. coli* catalyzed with different photocatalysts after being irradiated for a certain period; (c) photocatalytic antibacterial rates of different photocatalysts and (d) photographs for *E. coli* and *S. aureus* in the dark or under irradiation for 45 min; (e) SEM images of *E. coli* and *S. aureus* before and after being irradiated for 45 min with P7/g-C₃N₄.

no influence on the number of living bacteria in the dark but the decreases in the presence of Px/g-C₃N₄ could not be ignored (about 10%), which was caused by the antibacterial activities of the carbazole side-chained conjugated polymers. Moreover, the Px/g-C₃N₄ showed significantly enhanced photocatalytic antibacterial activities under light compared with g-C₃N₄, owing to the promoted charge separation and transfer and the enhanced light utilization. In general, the germicidal activity of the photocatalysts satisfied the following order: P7/g-C₃N₄ > P9/g-C₃N₄ > P5/g-C₃N₄ > P4/g-C₃N₄ > g-C₃N₄. Particularly, only few bacteria were detected in the group of P7/g-C₃N₄ under 45 min light irradiation, which was equivalent to an antibacterial rate of > 99.7% for both *E. coli* and *S. aureus*. By contrast, after being exposed to light for 45 min with g-C₃N₄, P4/g-C₃N₄, P5/g-C₃N₄, and P9/g-C₃N₄, the tested antibacterial rates were 22.2%, 60.4%, 92.2%, and 94.4% for *E. coli* and 20.8%, 63.6%, 91.4%, and 95.0% for *S. aureus*. This result was also evidently presented in the photographs of *E. coli* and *S. aureus* in Figs. 4b and 4d. The P7/g-C₃N₄ achieved the best photocatalytic antibacterial performance because of the relative balance between the extended light absorption and promoted charge separation. In contrast, even with the widest light absorption, the photocatalytic antibacterial activity of P4/g-C₃N₄ was the worst among the Px/g-C₃N₄, which was caused by the unsatisfactory charge separation and transfer and poor water wettability. Further, the comparison of the antibacterial performance of P7/g-C₃N₄ in this work with the previous photocatalysts based on g-C₃N₄ have been summarized in Table S2. The SEM was employed to further detect the antibacterial behavior of P7/g-C₃N₄. As shown in Fig. 4e, the *E. coli* and *S. aureus* possessed rod-shaped and sphere-shaped morphology, respectively, with intact structure and smooth surface without the photocatalytic treatment. Nevertheless, severe damages including depression, shrinkage and rupture occurred on the bacterial cell walls and membranes after being treated with P7/g-C₃N₄ under light irradiation for 45 min, indicating that the Px/g-C₃N₄ killed the bacteria by

destroying their cell walls and membranes.

3.3.2. Photocatalytic degradation of pollutants

The photocatalytic degradation curves of RhB by different photocatalysts are presented in Fig. 5a. The C_t is defined as the residual concentration of RhB at time t , while C_0 is the initial concentration. After the adsorption-desorption equilibrium, about 16% RhB was absorbed by g-C₃N₄, while for the Px/g-C₃N₄ systems, the concentration of RhB dropped by about 20%. In the blank group with only light, almost no concentration change of RhB was detected, which confirmed that the light itself had no effect on RhB degradation. In addition, it could be observed that all the Px/g-C₃N₄ heterostructures exhibited higher photocatalytic degradation activity in comparison to the pure g-C₃N₄, where only ~45.9% of RhB was decomposed under the identical condition in 90 min. The P7/g-C₃N₄ showed the highest photocatalytic activity among Px/g-C₃N₄, with a RhB degradation rate of 97.6% after being irradiated for 90 min. Compared with P7/g-C₃N₄, the photocatalytic activity of P9/g-C₃N₄ was slightly lower, where the degradation rate of RhB reached 92.3%. However, P4/g-C₃N₄ and P5/g-C₃N₄ were less photocatalytic reactive, which could decompose 80.0% and 87.0% of RhB, respectively. The comparison of the photocatalytic degradation performance of P7/g-C₃N₄ for RhB with the previous photocatalysts based on g-C₃N₄ have been summarized (Table S3). To study the performance of the photocatalysts in the real water sample, the RhB photocatalytic degradation test was conducted in the tap water. As shown in Fig. S7, the concentration changes of RhB in the blank system in the dark or light could be neglected, which was similar to the result in the deionized water. However, the degradation rates in the tap water catalyzed by g-C₃N₄ and P7/g-C₃N₄ decreased to 36.9% and 76.2%, respectively, after being irradiated for 90 min. This result may be caused by a combination of various factors such as solution pH, dissolved organic substances and inorganic species [45]. The degradation

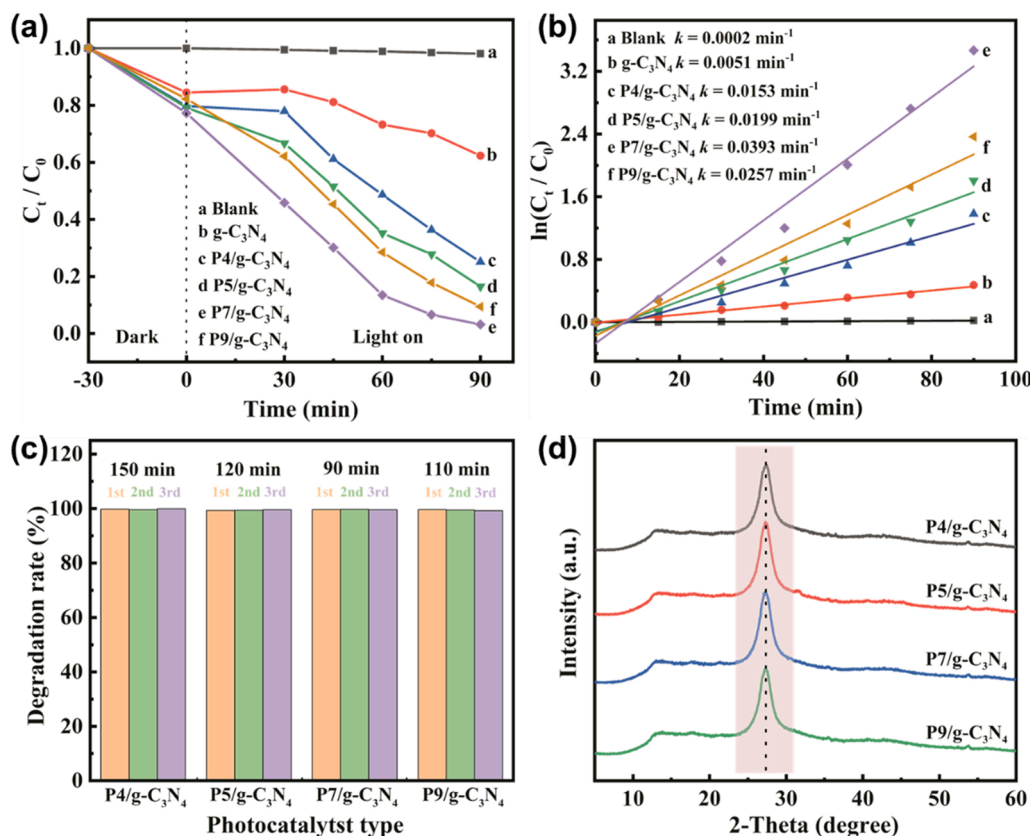


Fig. 5. (a) The degradation efficiencies and (b) degradation dynamic kinetic curves of RhB catalyzed by different photocatalysts; (c) the recycled photocatalytic degradation rates of RhB by Px/g-C₃N₄ under irradiation; (d) XRD patterns of Px/g-C₃N₄ PHJs after the third recycled photocatalytic degradation experiment.

dynamic kinetic curves of RhB catalyzed by different photocatalysts are shown in Fig. 5b. It could be observed that the degradation process of RhB was fitted well with the simplified Langmuir-Hinshelwood model with the equation of $-\ln(C_t/C_0) = kt$ (Here, C_0 corresponds to the concentration of RhB after the dark treatment) [46]. The reaction rate constants (k) of g-C₃N₄, P4/g-C₃N₄, P5/g-C₃N₄, P7/g-C₃N₄, and P9/g-C₃N₄ were 0.0051, 0.0153, 0.0199, 0.0393, and 0.0257 min⁻¹, respectively. Significantly, the k of P7/g-C₃N₄ was 7.7 times that of g-C₃N₄ and the above results were in good consistent with that of the photocatalytic sterilization. As the value of the total organic carbon (TOC) is an index to evaluate the mineralization of solution [45,47], the TOC test was conducted during the RhB degradation process in the P7/g-C₃N₄ group in deionized water. As shown in Fig. S8, the content of inorganic carbon (IC) is basically stable during the RhB degradation process, while the total carbon (TC) and TOC contents decreased with the reaction. After being irradiated for 90 min, the TOC removal rate reached 35.4%, which was lower than the degradation rate of RhB (97.6%). This result indicated that numbers RhB molecules were degraded to certain intermediates within 90 min and part RhB molecules were mineralized to CO₂ and H₂O. The stabilities of Px/g-C₃N₄ heterostructures were evaluated by the degradation experiments of RhB in three consecutive cycles. As shown in Fig. 5c, after three cycles, the photocatalytic activities of these PHJs showed no significant decrease, which satisfied the photocatalytic stability requirement for industrial

applications. Moreover, the XRD patterns of the Px/g-C₃N₄ heterostructures (Fig. 5d) were collected after the photocatalytic reactions. There was no detectable difference of the XRD patterns of Px/g-C₃N₄ before and after the photocatalytic degradation process, revealing their excellent crystal structure stability.

3.4. The photocatalytic mechanism and molecular design strategy

3.4.1. The Photocatalytic mechanism

To understand the formation of Px/g-C₃N₄ heterostructures at the molecular level, the ESP of Px and g-C₃N₄ in their optimized molecular were calculated. The ESP distributions and average ESP values on the atoms are shown in Fig. 6 and the atom labels of Px and g-C₃N₄ are presented in Fig. S9. It could be seen that most of the area on the main chains of Px exhibited negative ESP, while the positive ESP were mainly concentrated on the carbon atoms and hydrogen atoms of alkyl chains. For g-C₃N₄, the carbon atoms on the heptazine rings presented positive ESP, whereas the nitrogen atoms possessed negative ESP. Thereby, it was reasonable to assume that the intermolecular electric field was formed between the main chains of Px and the carbon atoms (label 1–6, 26–37, and 65–81) on the heptazine rings of g-C₃N₄, leading to enhanced electron transfer and excellent photocatalytic performance.

To clarify the reactive oxygen species (ROS) in the photocatalytic reactions, the active species capture experiments were conducted with

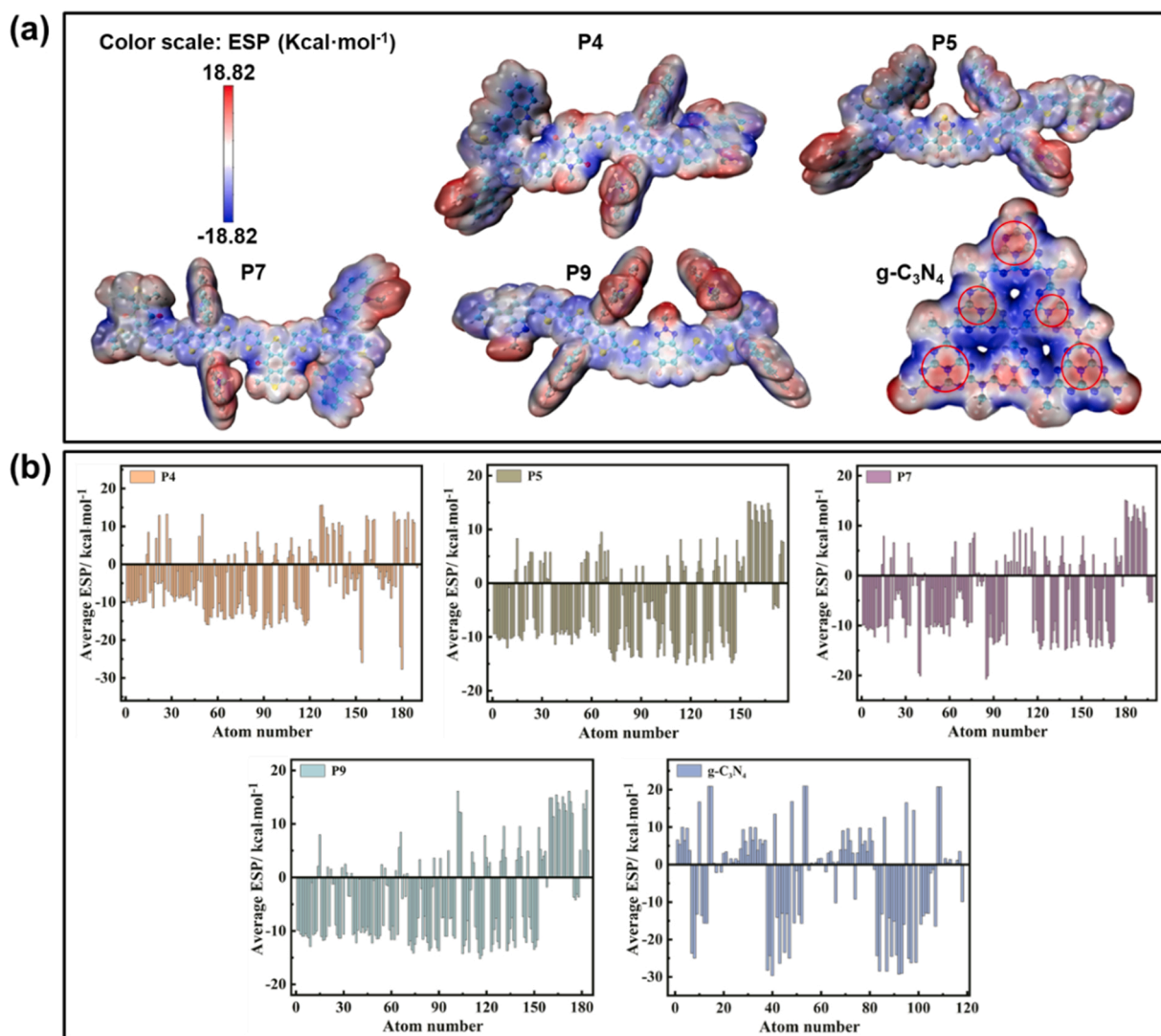


Fig. 6. (a) The ESP distributions on the van der Waals surface and (b) the average ESP values on the atoms of P4, P5, P7, P9, and g-C₃N₄.

different scavengers. The photocatalytic degradation experiments with different scavengers under light for 90 min are illustrated in Fig. 7a. It could be seen that the degradation rates of RhB by g-C₃N₄ and P7/g-C₃N₄ occurred the most significantly decrease when the TEMPOL was added, revealing that $\cdot\text{O}_2^-$ was the most critical active species determining the photocatalytic degradation efficiency. Besides, the degradation rates decreased from 93.8% and 39.4% to 90.6% and 33.0% in the P7/g-C₃N₄ and g-C₃N₄ systems, respectively, in the presence of Sodium oxalate, suggesting that the h^+ also promoted the photocatalytic degradation reaction but not as significant as the $\cdot\text{O}_2^-$. In contrast, the degradation rates were not affected by the addition of IPA, which indicated that the $\cdot\text{OH}$ did not contribute to the degradation of RhB. Figs. 7b and 7c presented the effect of the scavengers on the antibacterial activities of the photocatalysts toward the *S. aureus*. For the g-C₃N₄ and P7/g-C₃N₄ system, conspicuous loss of antibacterial rates occurred

after the introduction of TEMPOL, demonstrating the important role of $\cdot\text{O}_2^-$ in the photocatalytic antibacterial process. In addition, the decrease of antibacterial rates caused by the addition of Sodium oxalate could not be neglected, which suggested that the h^+ may contribute to the photocatalytic reaction to a certain extent. Nevertheless, the photocatalytic antibacterial activity of the photocatalysts remained unchanged after adding IPA, which indicated that few $\cdot\text{OH}$ were generated in the photocatalytic process. This result was in good consistent with that of the photocatalytic degradation. To further probe the ROS generation in the photocatalytic reactions, the ESR measurement was performed with the 5,5-dimethyl-1-pyrroline N-oxide (DMPO) as the trapping agent of $\cdot\text{O}_2^-$ and $\cdot\text{OH}$. As illustrated in Fig. 7d, P7/g-C₃N₄ and g-C₃N₄ showed a 1:1:1:1 quartet for DMPO- $\cdot\text{O}_2^-$ adduct after being irradiated for 1 min. However, the intensity of the signal observed in g-C₃N₄ was much weaker, which demonstrated that the P7/g-C₃N₄ could

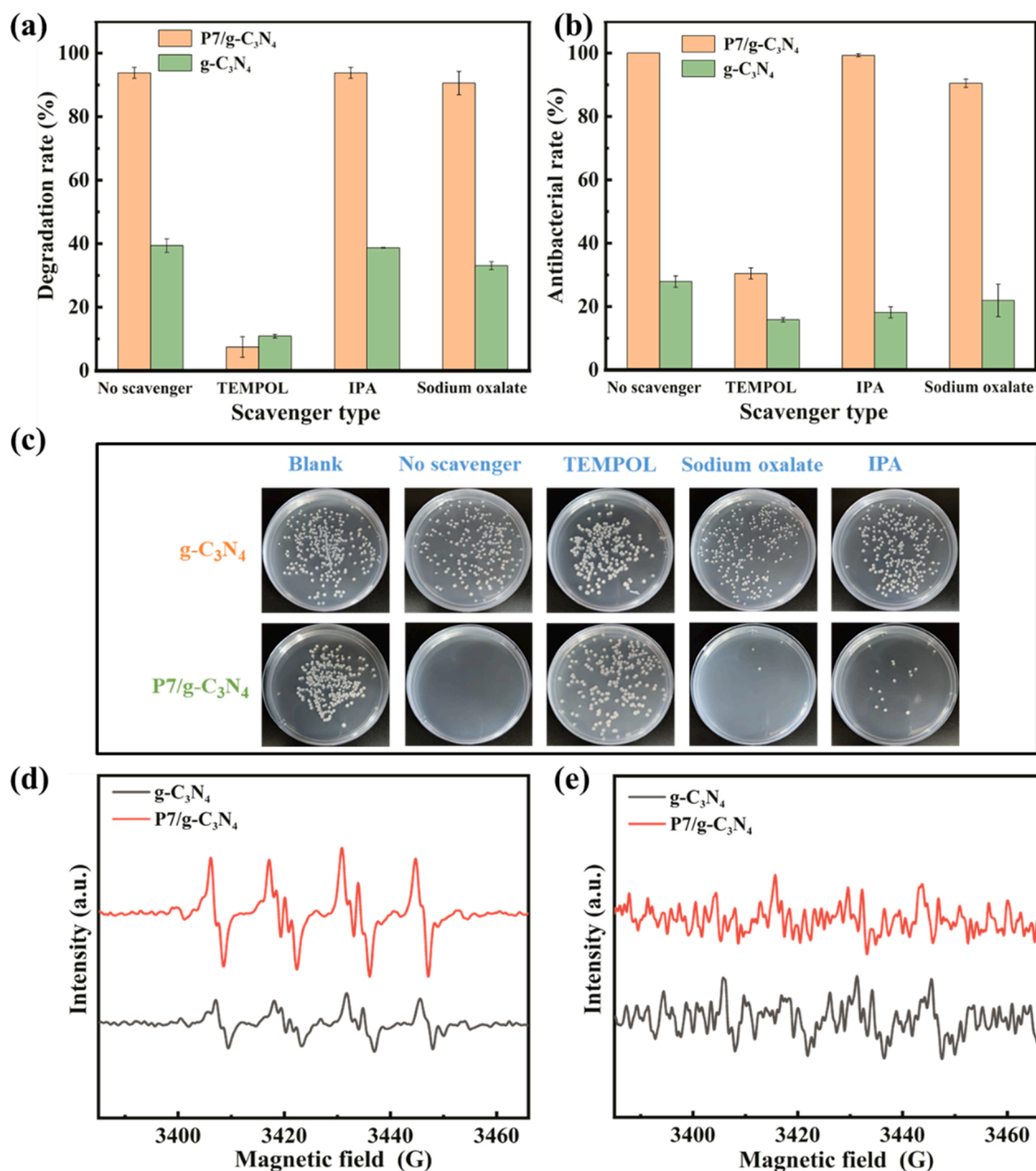


Fig. 7. (a) The degradation rates of RhB by g-C₃N₄ and P7/g-C₃N₄ with different scavengers under light for 90 min; (b) photocatalytic antibacterial rates of g-C₃N₄ and P7/g-C₃N₄ and (c) photographs for *S. aureus* after irradiation for 60 min with different scavengers; ESR spectra of g-C₃N₄ and P7/g-C₃N₄ for detection of (d) $\cdot\text{O}_2^-$ and (e) $\cdot\text{OH}$ after being irradiated for 60 s with DMPO as the active free radicals trapping agent.

produce more $\cdot\text{O}_2^-$ than the g-C₃N₄, leading to enhanced photocatalytic activity. Since the $\cdot\text{O}_2^-$ was produced by the reaction of free electrons with the oxygen, it could be concluded that more electrons were generated in P7/g-C₃N₄ than in g-C₃N₄, implying more efficient separation and transfer of the photo-induced charges in the former. Nevertheless, the characteristic peaks for DMPO- $\cdot\text{OH}$ were too weak to detect in both P7/g-C₃N₄ and g-C₃N₄ systems (Fig. 7e), suggesting that few $\cdot\text{OH}$ were generated in the photocatalytic process. This was caused by the lower HOMO level potentials of g-C₃N₄ and Px than the standard redox potential of $\text{OH}^-/\cdot\text{OH}$, which makes the h^+ could not oxidize OH^- to $\cdot\text{OH}$. As demonstrated by the literatures [48,49], the H_2O_2 generated by the further reduction of $\cdot\text{O}_2^-$ was another crucial ROS that could promote the proceed of photocatalytic reactions. Thereby, the H_2O_2 evolution activity of g-C₃N₄ and Px/g-C₃N₄ PHJs was tested. As shown in Fig. S10, the Px/g-C₃N₄ produced more H_2O_2 than the pure g-C₃N₄ with continued irradiation, which was beneficial to enhance the photocatalytic activity. Particularly, the H_2O_2 evolution activity of the photocatalysts satisfied the order: P7(P9)/g-C₃N₄ > P5/g-C₃N₄ > P4/g-C₃N₄ > g-C₃N₄.

Based on the energy level arrangement states between Px and g-C₃N₄, and the related results and analysis above, the photocatalytic mechanisms of Px/g-C₃N₄ PHJs were proposed. For both g-C₃N₄ and Px, after being irradiated, the dissociated electrons would transfer to the LUMO levels and the holes would be left in the HOMO levels. Unfortunately, the excitons generated by g-C₃N₄ and Px are prone to recombine, resulting in poor photocatalytic performance. Driven by Type I band alignment between g-C₃N₄ and P4 (P5), the photogenerated electrons and holes in g-C₃N₄ would transfer to the LUMO and HOMO levels of P4 (P5), respectively, with different migration rates and transfer distance. In contrast, as shown in Fig. 8, the Type II band alignment between g-C₃N₄ and P7 (P9) would drive the electrons in P7 (P9) to the LUMO level of g-C₃N₄, and the holes in g-C₃N₄ to the HOMO levels of P7 (P9), leading to more effective charge separation. Then, the photo-induced electrons in the PHJs would reduce O_2 to generate the $\cdot\text{O}_2^-$ and part $\cdot\text{O}_2^-$ would be further reduced to H_2O_2 [50], which together with the holes would kill the bacteria and degrade the organic pollutants. Overall, in comparison to pure g-C₃N₄, the charge separation and transfer was promoted in the Px/g-C₃N₄ PHJs and the P7(P9)/g-C₃N₄ were more effective in inhibiting the charge recombination than the P4 (P5)/g-C₃N₄ PHJs.

3.4.2. The molecular design strategy

The molecular design strategy of the Px/g-C₃N₄ heterostructures is proposed and presented in Fig. 9. The molecular energy levels of Px/g-C₃N₄ were engineered for more efficient charge separation and wider light absorption by introducing different A units. After DPP and DTffBT with relative stronger electron-withdrawing ability were selected as the A units in P4 and P5, the absorption edge of the PHJs was bathochromic-

shifted from 450 to 880 and 710 nm, which were larger than those of P7/g-C₃N₄ (650 nm) and P9/g-C₃N₄ (620 nm). Alternatively, copolymerizing the BDD and FBTA unit into the BDT-based backbone significantly promoted charge separation and transfer within the P7/g-C₃N₄ and P9/g-C₃N₄ due to the formation of Type II heterostructures.

The developed Px/g-C₃N₄ PHJs in this work have several advantages: (i) easily tuned energy levels through molecular design; (ii) strong response to the visible light for efficiently photocatalytic sterilization and degradation; (iii) low toxicity and environmental friendliness; (iv) excellent cyclic stability. The subsequent research needs to solve the hydrophobicity of the PHJs to improve the catalyst-water interface for the practical application. Besides, the separation and reuse of the PHJs powders from the treated water also requires to be studied. Immobilizing the photocatalysts on the substrates or coupling them in the reactors are potential methods to address the problems above [51,52].

4. Conclusions

In summary, four BDT-based conjugated polymers Px were synthesized and combined with g-C₃N₄ to fabricate PHJs (Px/g-C₃N₄) for photocatalytic sterilization and degradation. The carbazole side-chain helps Px absorb the blue and ultraviolet light and also gives Px the antibacterial property. The main chain copolymerization with different A units contributes to adjust the energy levels of Px to make a better use of the light with long wavelengths. It revealed that these Px/g-C₃N₄ exhibited significantly higher photocatalytic activity than the pure g-C₃N₄. Specifically, the P7/g-C₃N₄ with BDD as the A unit of P7 showed the highest photocatalytic activity with an over 99.7% antibacterial rates for *E. coli* and *S. aureus* and 97.6% degradation rate for RhB after being irradiated for 45 and 90 min, respectively. These excellent results were competitive with those of the previous reported work and could be ascribed to the relative balance between light absorption, charge separation efficiency, and water wettability of P7/g-C₃N₄. Therefore, it is feasible to regulate the molecular energy levels by rational molecular design for developing environment-friendly PHJs to achieve excellent photocatalytic sterilization and degradation performance.

CRediT authorship contribution statement

Xiaojie Liu: Conceptualization, Methodology, Formal analysis, Investigation, Data curation, Writing – original draft. **Yahui Du:** Formal analysis, Data curation. **Yong Zhao:** Writing – review & editing. **Xin Song:** Methodology, Formal analysis. **Xin Jing:** Software. **Liangmin Yu:** Project administration, Supervision. **Mingliang Sun:** Resources, Supervision, Project administration, Funding acquisition.

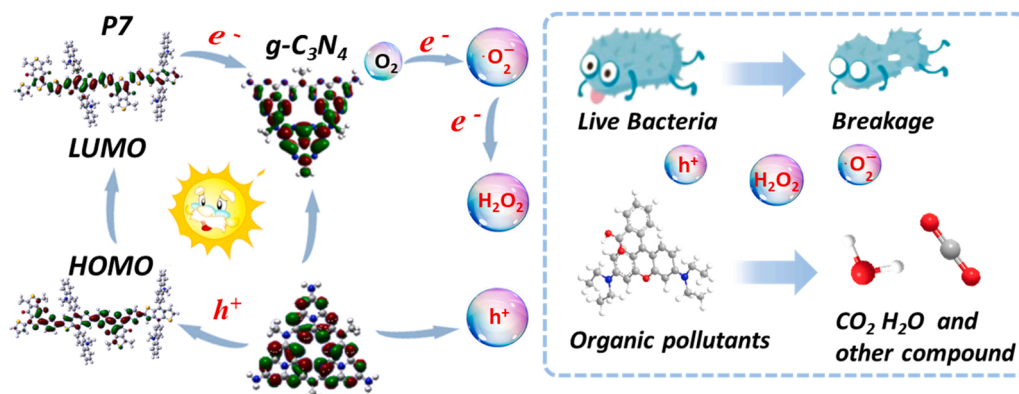


Fig. 8. The photocatalytic mechanism diagram of P7/g-C₃N₄.

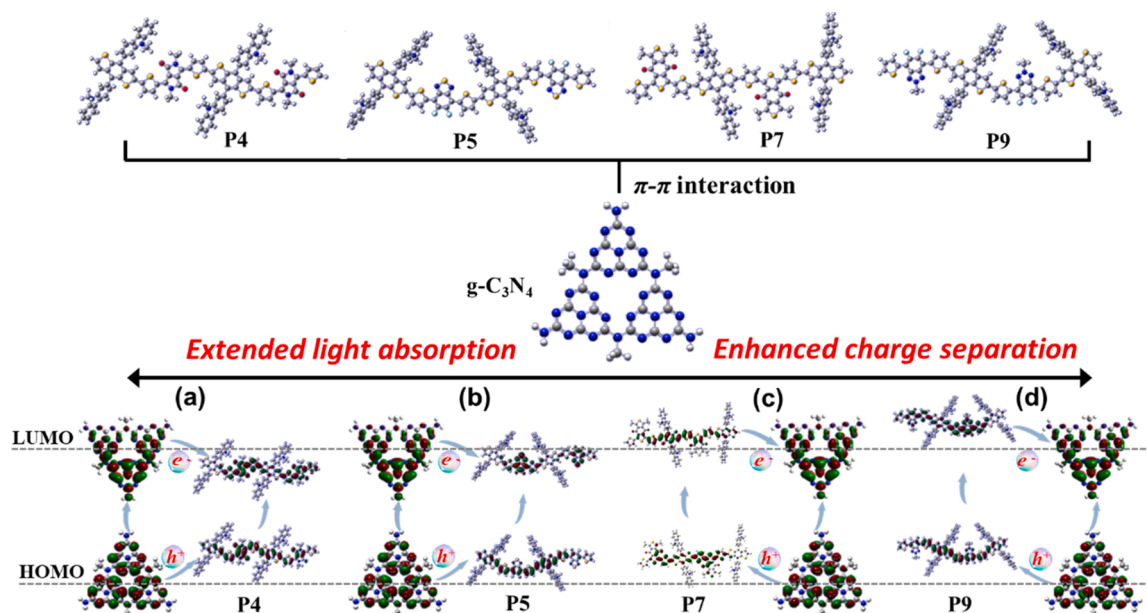


Fig. 9. The molecular design strategy of (a) P4/g-C₃N₄, (b) P5/g-C₃N₄, (c) P7/g-C₃N₄, and (d) P9/g-C₃N₄.

Declaration of Competing Interest

The authors declare that they have no known competing financial interests or personal relationships that could have appeared to influence the work reported in this paper.

Acknowledgments

This work was supported by the National Natural Science Foundation of China (52173291, U1806223), and Open Fund of the State Key Laboratory of Luminescent Materials and Devices (South China University of Technology, 2021-skllmd-11).

Appendix A. Supporting information

Supplementary data associated with this article can be found in the online version at doi:10.1016/j.apcatb.2022.121401.

References

- [1] X. Kong, X. Liu, Y. Zheng, P.K. Chu, Y. Zhang, S. Wu, *Mat. Sci. Eng. R.* 145 (2021), 100610.
- [2] X. Zhang, F. Tian, X. Lan, Y. Liu, W. Yang, J. Zhang, Y. Yu, *Chem. Eng. J.* 429 (2022), 132588.
- [3] Z. Zhang, Y. Wang, W. Teng, X. Zhou, Y. Ye, H. Zhou, H. Sun, F. Wang, A. Liu, P. Lin, W. Cui, X. Yu, Y. Wu, Z. Ye, *Biomaterials* 274 (2021), 120853.
- [4] M. Berkani, A. Smaali, Y. Kadmi, F. Almomani, Y. Vasseghian, N. Lakhdari, M. Alyane, *J. Hazard. Mater.* 421 (2022), 126719.
- [5] P. Xia, S. Cao, B. Zhu, M. Liu, M. Shi, J. Yu, Y. Zhang, *Angew. Chem. Int. Ed.* 59 (2020) 5218–5225.
- [6] R. Wang, M. Shi, F. Xu, Y. Qiu, P. Zhang, K. Shen, Q. Zhao, J. Yu, Y. Zhang, *Nat. Commun.* 11 (2020) 4465.
- [7] L. Shi, Z. Ma, W. Qu, W. Zhou, Z. Deng, H. Zhang, *Appl. Surf. Sci.* 568 (2021), 150923.
- [8] D. Ayodhya, G. Veerabhadram, *Mater. Today Commun.* 19 (2019) 157–169.
- [9] Y. Lou, J. Liu, M. Liu, F. Wang, *ACS Catal.* 10 (2020) 2443–2451.
- [10] P. Lou, J.Y. Lee, *ACS Appl. Mater. Interfaces* 12 (2020) 14289–14297.
- [11] X. Wang, K. Maeda, A. Thomas, K. Takanabe, G. Xin, J.M. Carlsson, K. Domen, M. Antonietti, *Nat. Mater.* 8 (2009) 76–80.
- [12] Q. Zhu, Z. Xu, B. Qiu, M. Xing, J. Zhang, *Small* 17 (2021) 2101070.
- [13] J. Gao, F. Zhang, H. Xue, L. Zhang, Y. Peng, X. Li, Y. Gao, N. Li, L. Ge, *Appl. Catal. B* 281 (2021), 119509.
- [14] W. Wang, G. Li, T. An, D.K.L. Chan, J.C. Yu, P.K. Wong, *Appl. Catal. B* 238 (2018) 126–135.
- [15] K. Wang, H. Wang, Q. Cheng, C. Gao, G. Wang, X. Wu, *J. Colloid Inter. Sci.* 607 (2022) 1061–1070.
- [16] J. Xiao, Q. Liu, M. Song, X. Li, Q. Li, J.K. Shang, *Water Res.* 198 (2021), 117125.

- [17] M. Liu, Y. Jiao, J. Qin, Z. Li, J. Wang, *Appl. Surf. Sci.* 541 (2021), 148558.
- [18] J. Fu, J. Yu, C. Jiang, B. Cheng, *Adv. Energy Mater.* 8 (2018) 1701503.
- [19] X. Zhou, Y. Liu, Z. Jin, M. Huang, F. Zhou, J. Song, J. Qu, Y.J. Zeng, P.C. Qian, W. Y. Wong, *Adv. Sci.* 8 (2021) 2002465.
- [20] Y. Du, X. Liu, Q. Wang, L. Yu, L. Chu, M. Sun, *J. Colloid Inter. Sci.* 608 (2021) 103–113.
- [21] Z. Fu, A. Vogel, M.A. Zwijnenburg, A.I. Cooper, R.S. Sprick, *J. Mater. Chem. A* 9 (2021) 4291–4296.
- [22] C. Dai, B. Liu, *Energy Environ. Sci.* 13 (2020) 24–52.
- [23] T. Yang, E. Zhu, H. Guo, J. Du, Y. Wu, C. Liu, G. Che, *ACS Appl. Mater. Interfaces* 13 (2021) 51447–51458.
- [24] Z. Wang, X. Zheng, P. Chen, D. Li, Q. Zhang, H. Liu, J. Zhong, W. Lv, G. Liu, *J. Hazard. Mater.* 424 (2022), 127379.
- [25] D. Dang, D. Yu, E. Wang, *Adv. Mater.* 31 (2019) 1807019.
- [26] W. Zhou, T. Jia, H. Shi, D. Yu, W. Hong, X. Chen, *J. Mater. Chem. A* 7 (2019) 303–311.
- [27] W. Zhou, Z. Hu, F. Huang, W. Hong, X. Chen, *Appl. Catal. B* 270 (2020), 118852.
- [28] J. Chen, C.L. Dong, D. Zhao, Y.C. Huang, X. Wang, L. Samad, L. Dang, M. Shearer, S. Shen, L. Guo, *Adv. Mater.* 29 (2017) 1606198.
- [29] H. Yao, L. Ye, H. Zhang, S. Li, S. Zhang, J. Hou, *Chem. Rev.* 116 (2016) 7397–7457.
- [30] C. Cui, Y. Li, *Energy Environ. Sci.* 12 (2019) 3225–3246.
- [31] J. Hou, M.-H. Park, S. Zhang, Y. Yao, L.-M. Chen, J.-H. Li, Y. Yang, *Macromolecules* 41 (2008) 6102–6108.
- [32] F. Li, X. Song, K. Zhang, B. Shahid, Q. Wang, L. Yu, D. Zhu, M. Sun, *Dyes Pigments* 170 (2019), 107548.
- [33] S.-L. Zhou, H.-L. Tang, M. Yao, S.-N. Cao, L.-Y. Zhuang, C.-S. Cao, Y.-H. Shi, *Chem. Pap.* 73 (2019) 2477–2484.
- [34] J. Liu, H. Li, H. Li, S. Fang, J. Shi, Y. Chen, R. Zhong, S. Liu, S. Lin, *J. Med. Chem.* 64 (2021) 10429–10444.
- [35] T. Lu, F. Chen, *J. Comput. Chem.* 33 (2012) 580–592.
- [36] T. Lu, S. Manzetti, *Struct. Chem.* 25 (2014) 1521–1533.
- [37] T. Lu, F. Chen, *J. Mol. Graph. Model.* 38 (2012) 314–323.
- [38] J. Zhang, T. Lu, *Phys. Chem. Chem. Phys.* 23 (2021) 20323–20328.
- [39] H. Ye, Z. Wang, F. Yu, S. Zhang, K. Kong, X. Gong, J. Hua, H. Tian, *Appl. Catal. B* 267 (2020), 118577.
- [40] F. Yu, Z. Wang, S. Zhang, H. Ye, K. Kong, X. Gong, J. Hua, H. Tian, *Adv. Funct. Mater.* 28 (2018) 1804512.
- [41] Y. Deng, J. Liu, Y. Huang, M. Ma, K. Liu, X. Dou, Z. Wang, S. Qu, Z. Wang, *Adv. Funct. Mater.* 30 (2020) 2002353.
- [42] K. Dou, X. Wang, Z. Du, H. Jiang, F. Li, M. Sun, R. Yang, *J. Mater. Chem. A* 7 (2019) 958–964.
- [43] X. Liu, X. Jing, Y. Zhao, W. Wang, L. Yu, M. Sun, *A.C.S. Appl. Electron. Mater.* 2 (2020) 4012–4022.
- [44] J. Duan, Y. Zhao, Y. Wang, X. Yang, Q. Tang, *Angew. Chem. Int. Ed.* 58 (2019) 16147–16151.
- [45] H. Wang, Y. Wu, M. Feng, W. Tu, T. Xiao, T. Xiong, H. Ang, X. Yuan, J.W. Chew, *Water Res.* 144 (2018) 215–225.
- [46] X. She, H. Xu, H. Wang, J. Xia, Y. Song, J. Yan, Y. Xu, Q. Zhang, D. Du, H. Li, *Dalton Trans.* 44 (2015) 7021–7031.
- [47] H. Wang, J. Zhang, X. Yuan, L. Jiang, Q. Xia, H. Chen, *Chem. Eng. J.* 392 (2020), 123638.
- [48] D. He, Z. Zhang, Y. Xing, Y. Zhou, H. Yang, H. Liu, J. Qu, X. Yuan, J. Guan, Y.-n Zhang, *Chem. Eng. J.* 384 (2020), 123258.

- [49] C. Hu, H. Huang, F. Chen, Y. Zhang, H. Yu, T. Ma, *Adv. Funct. Mater.* 30 (2019) 1908168.
- [50] W. Wang, W. Gu, G. Li, H. Xie, P.K. Wong, T. An, *Environ. Sci.: Nano* 7 (2020) 3877–3887.
- [51] C. Zhang, Y. Li, J. Li, *Chem. Eng. J.* 392 (2020), 123687.
- [52] C. Zhang, M. Zhang, Y. Li, D. Shuai, *Appl. Catal. B* 248 (2019) 11–21.